



UFR
Sciences
& Techniques



Magnetic Turbulence in Solar Wind

Project Report

DE GELIS Pierre-Marie
M2 Space Sciences and Applications

Project Tutor:

Dr. Matthieu KRETZSCHMAR / Professor at Université d'Orléans

Laboratoire de Physique et Chimie de l'Environnement et de l'Espace (LPC2E)
Period: November - February 2025

2024-2025

Table of Contents

1	Introduction	1
2	Methods	2
2.1	Waves Presence at the Cyclotronic Scale	2
2.2	Data Set - RTN Magnetic Field	2
2.3	Analysis Tools	3
2.3.1	Power Spectral Density: Energetic Cascade	3
2.3.2	Merge Noise & PSD Noise Reduction	3
2.3.3	Reduced Magnetic Helicity: Wave Identification	4
3	Results	6
3.1	Cascade Interruption	6
3.2	Whistler Waves Considerations	6
4	Conclusion & Perspectives	7
5	Appendices	8
5.1	Appendix A: Magnetic Field Evolution of Others Days	8
5.2	Appendix B: Reduced Magnetic Helicity Demonstration	8
5.3	Appendix C: Polarization Consideration	9
5.4	Appendix D : Analytical Derivation of the Rotation Matrix	9
5.5	Appendix E : Spectrograms of others days	10
5.6	Appendix F : Mean helicity and mean PSD over time for all days	11
5.7	Appendix G: PSD & Reduced Magnetic Helicity for Cyclotron and Whistler Wave Observations	12

1 Introduction

Turbulence is a fascinating phenomenon that exhibits similar statistical behaviors across various fields of physics, such as hydrodynamics and aerodynamics. It is characterized by a nonlinear transfer of energy from large scales, where energy is injected, to smaller scales, where it is dissipated. This process, known as the energy cascade, is marked by a progressive increase in frequency as energy moves to smaller spatial scales. At its core, turbulence is a chaotic process, sensitive to initial conditions and exhibiting complex, multi-scale interactions that make it both challenging and rich to study.

In the solar wind, turbulence plays a crucial role in the dynamics of the interplanetary medium, a plasma flow continuously emitted by the Sun. This turbulence is characterized by distinct regimes defined by characteristic scales. At frequencies higher than the ion cyclotron frequency (Eq.1), kinetic effects dominate, while at lower frequencies, the plasma behavior can be accurately modeled using the Magnetohydrodynamic (MHD) approximation. The ion cyclotron frequency is given by :

$$f_c = \frac{|q|B}{2\pi m} \quad (1)$$

In the MHD inertial range ($f \ll f_c$), the turbulence follows a Kolmogorov-like cascade [1] [2] with nonlinear interactions between Alfvénic fluctuations, [3] leading to a power spectrum :

$$E(k) \sim \varepsilon^{2/3} k^{-5/3} \quad (2)$$

where ε is the energy transfer rate and k is the wavenumber. The magnetic field spectral index typically varies from $-5/3$ to $-3/2$ in the solar wind [4].

At kinetic scales, comparable to or smaller than the ion inertial length or ion gyroradius, the fluid description breaks down. This transition is marked by a spectral break and steeper scaling :

$$E(k) \sim k^\alpha$$

where $\alpha \in [-3.1, -2.3]$ [5]. This regime involves various dissipation mechanisms, including ion cyclotron damping, Landau damping, and turbulent heating.

Data from Parker Solar Probe (PSP) led to a groundbreaking discovery in 2022 by Trevor Bowen : the identification of ion-scale waves near the cyclotron frequency that disrupt the turbulent energy cascade at kinetic scales, marking a key transition where energy is dissipated [6] [7].

The turbulent magnetic field in the near-Sun environment is measured by the complementary Magnetometer (MAG) and Search-Coil Magnetometer (SCM) [8] instruments aboard the Solar Orbiter mission. The SCM, for which the LPC2E is responsible, is specifically designed to capture high-frequency fluctuations, while the MAG measures slower variations. This analysis will be conducted using a unique merged dataset, combining measurements from both magnetometers. The key question is whether we can confirm these results using this unprecedented dataset.

The Laboratory of Physics and Chemistry of the Environment and Space (LPC2E) is a CNRS-affiliated research institute located in Orléans, France. It brings together interdisciplinary research teams specializing in Astrophysics, Atmospheric Environment, and Space Plasmas. This work was conducted within the Space Plasmas team under the supervision of Dr. Kretzschmar.

This project aims to reproduce Bowen's discovery using the merged Solar Orbiter data and to develop an analysis program for observation and measurement of these phenomena. More broadly, this research will serve as a foundation for developing analysis interfaces to facilitate future studies in turbulence. Ultimately, this endeavor explores solar wind turbulence, a growing field with many unanswered questions, hoping to discover new insights and guide future investigations.

Program & Documentation are available on Github :



2 Methods

2.1 Waves Presence at the Cyclotronic Scale

On January 23, 2024, a discovery published in *Nature Astronomy* by a team led by Bowen provides insight into what may cause the transition between these two scales [6]. The article demonstrates that ion cyclotron waves play a significant role in dissipation and plasma heating in the solar wind. More specifically, it highlights strong correlations between the power drop and the presence of left-handed waves corresponding to cyclotron waves (Figure 1). Their research revealed that these correlations can be quantified using the Spearman ranked correlation coefficient, showing values of $R = -0.5$ for the transition range and $R = -0.7$ for the inertial to kinetic range. Furthermore, the study found that circularly polarized power is often associated with higher cross-helicity, suggesting a complex interplay between wave activity and turbulent dynamics. These findings highlight that left-handed waves serve as a crucial pathway to dissipation, particularly in high-cross-helicity states.

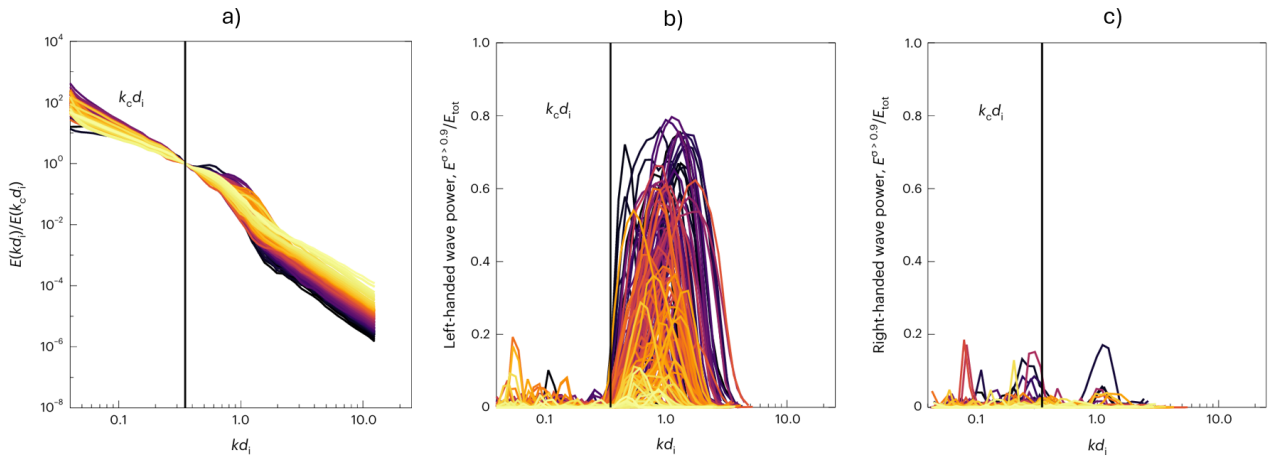


Figure 1: (a) Turbulent spectra normalized at $k_c d_i = 0.35$, color-coded by energy variation \tilde{E}_{TK} . Darker colors indicate a greater drop in power. (b) Circularly polarized power in left-handed modes normalized to the total power. (c) Circularly polarized power in right-handed modes normalized to the total power. from [6]

Figure 1 : (a) Turbulent spectra normalized at $k_c d_i = 0.35$, color-coded by energy variation \tilde{E}_{TK} . Darker colors indicate a greater drop in power. (b) Circularly polarized power in left-handed modes normalized to the total power. (c) Circularly polarized power in right-handed modes normalized to the total power. [Bowen, 2024]

It is this critical role of left-handed waves in the dissipation process that we aim to emphasize.

2.2 Data Set - RTN Magnetic Field

The magnetic field data is provided in the Radial-Tangential-Normal (RTN) coordinate system, where B_R (radial, Sun to spacecraft), B_T (tangential, \perp to radial and \parallel to solar equator), and B_N (normal, completing the orthogonal frame) are measured in nanoTesla (nT) and sampled at 256 Hz.

The data combines measurements from Solar Orbiter's Magnetometer (MAG) and the Radio and Plasma Waves (RPW) Search Coil Magnetometer (SCM), ensuring broad frequency coverage. Data quality is indicated by bitmasks and flags. This work analyzes measurements from 9 August 2021, 6 September 2022, and 4 April 2024.

We focus on the first day shown in Figure 2, while the other two days are provided in Appendix A Figure 8. We can observe that the field is not continuous. The missing data are due to the SCM not observing during this period (no high-frequency data), although MAG data are available. The shock we observe is likely caused by a coronal mass ejection, a dense cloud of plasma with high velocity (~ 1000 km/s) that compresses the solar wind plasma.

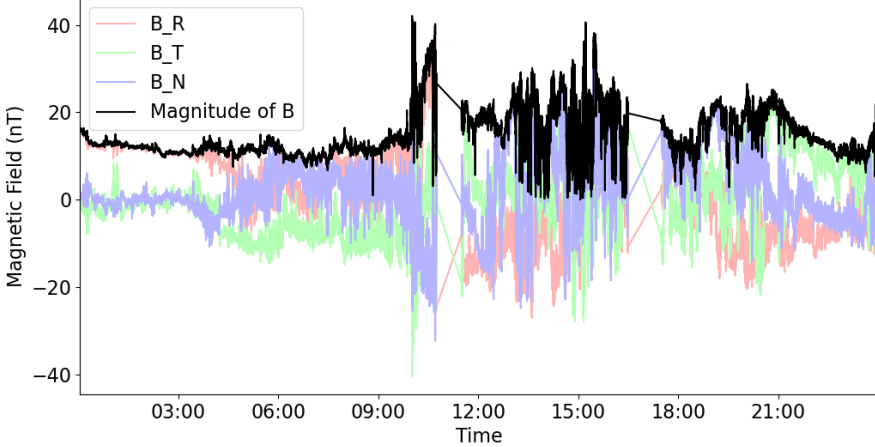


Figure 2: Magnetic Field Evolution of 6 September 2022 in RTN coordinates

2.3 Analysis Tools

2.3.1 Power Spectral Density: Energetic Cascade

To analyze the distribution of magnetic energy across different frequencies, we compute the Power Spectral Density (PSD) using Welch's method [9]. This technique involves dividing the time series into overlapping segments and applying several processing steps to ensure robust spectral estimates.

For each magnetic field component, we first divide the data into segments with an overlap between consecutive segments. For each segment, Welch computes averaged periodograms to reduce variance in the spectral estimates and applying a Hann window to each segment before computing the Fourier transform.

The total magnetic power spectral density is given by :

$$\text{PSD}_{\text{total}}(f) = \text{PSD}_{B_R}(f) + \text{PSD}_{B_T}(f) + \text{PSD}_{B_N}(f) \quad (3)$$

With this method, we recover the $-5/3$ power law associated with the fluid regime, as well as the $-8/3$ power law associated with the kinetic regime, as shown in Figure 3a.

The spectrogram in Figure 5a) reveals the energy distribution across frequencies, enhanced by frequency compensation (f^3), logarithmic transformation, and adaptive normalization. It shows time evolution on the x-axis, logarithmic frequency scale (0.1 to 100 Hz) on the y-axis, and normalized PSD intensity in color. Negative values (blue) indicate low spectral power, while positive values (yellow) denote significant energy peaks, enabling the tracking of structures across spatial scales.

2.3.2 Merge Noise & PSD Noise Reduction

In order to definitively identify significant signals within the data, we must precisely characterize the background noise. In Fourier space, the noise follows a Gaussian distribution whose variance is proportional to the square of the Fourier coefficients (PSD). This fundamental property stems directly from Parseval's theorem, which relates the signal energy in the time domain to that in the frequency domain. To discriminate physical signals from background noise, we establish a detection threshold at 3σ (three standard deviations) above the median noise curve. Figure 3b shows the noise power spectrum (blue curve) along with the $\pm 3\sigma$ confidence bands (colored areas). This visualization allows us to clearly identify the range of expected statistical fluctuations: any signal exceeding the upper band ($+3\sigma$) is considered potentially significant.

In order to improve the data quality, we have to reduce noise. To do that, we can implement a threshold in the PSD segments to keep only segments that exceed the noise in a certain frequency range (Figure 4). The threshold definition depends on our data and has to be adapted. Here, we selected PSD segments that exceed the noise in the 7.75-100 Hz range.

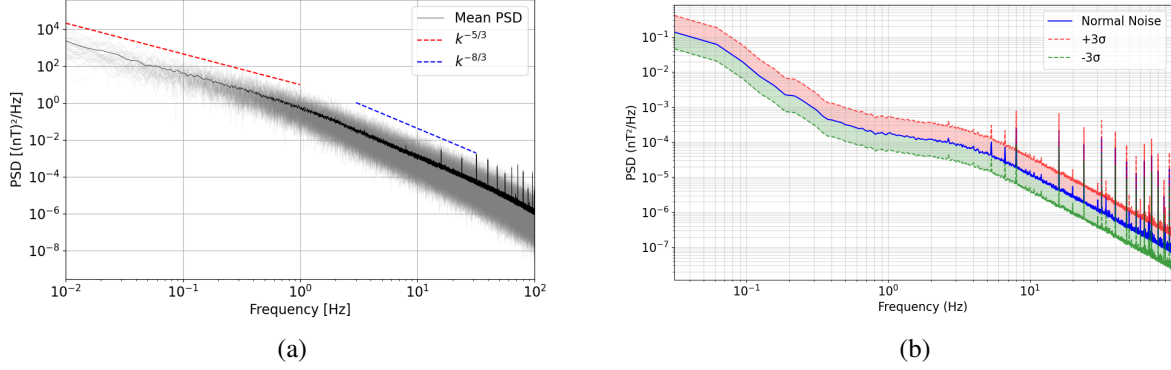


Figure 3: **a)** Power Spectral Density of 6 September 2022 between 1 to 4 PM / Conditions : size of segment : 100000 points and overlap 50000 points ; **b)** Merge Noise with $\pm 3\sigma$ Fluctuations

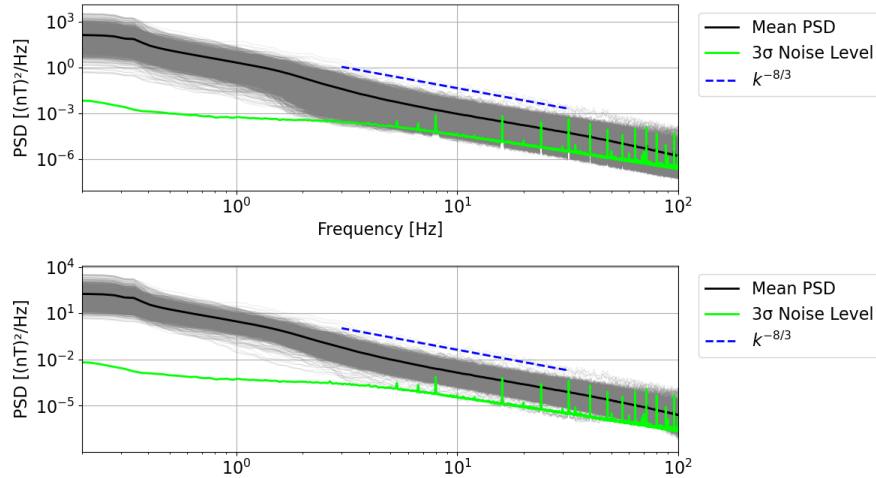


Figure 4: Segment size : 8192 points ; Overlap : 6553.6 points ; **Top** : 4462 PSD segments and average before threshold implementation for the 4 April 2024 ; **Bottom** : 3467 PSD segments after threshold implementation

2.3.3 Reduced Magnetic Helicity: Wave Identification

Reduced magnetic Helicity

To identify left-handed cyclotron waves mentioned in the article, we analyze the transverse plane of the magnetic field. For this purpose, we use the reduced magnetic helicity [10] [11], as detailed in Appendix B :

$$\langle \sigma_m \rangle = \frac{2\text{Im}\langle b_T^* b_N \rangle}{\langle b_T^2 + b_N^2 \rangle} \quad (4)$$

where b_T and b_N are the Fourier coefficients of the magnetic field components, and $*$ denotes the complex conjugate.

This expression provides insights into the circular polarization of the waves. Specifically:

- Positive helicity ($\langle \sigma_m \rangle > 0$) corresponds to left-handed circularly polarized waves.
- Negative helicity ($\langle \sigma_m \rangle < 0$) corresponds to right-handed circularly polarized waves.

The interpretation of helicity can be demonstrated using the reference frame described in Appendix C. In this frame, we assume the wave vector \mathbf{k} is aligned with the positive radial direction (parallel to the background magnetic field). This alignment simplifies the analysis of the transverse plane (T, N). In this configuration,

waves propagating with counterclockwise polarization in the transverse plane are associated with negative helicity and are thus left-handed circularly polarized. However, the observed polarization is dependent on the sign of $\mathbf{k} \cdot \mathbf{V}_{sw}$, where \mathbf{V}_{sw} is the solar wind velocity [12]. The polarization of ion-resonant and electron-resonant waves will be reversed in the spacecraft frame if $\mathbf{k} \cdot \mathbf{V}_{sw} < 0$.

For the magnetic helicity calculation, we process the same data segments using a direct Fast Fourier Transform (FFT) approach. The segmentation and windowing procedures remain identical to those used in previous analyses to ensure consistency. However, the FFT is applied directly to the windowed data, preserving the phase information essential for accurate helicity calculations.

Figure 5b) confirms the presence of two types of waves: cyclotron waves in red near the cyclotron frequency ($f_c \approx 0.6$ Hz) and whistler waves in blue near 20-30Hz. If the waves are not exactly at the cyclotron frequency, this could be due to a Doppler shift [13].

Rotation Matrix for Magnetic Field Alignment

The rotation matrix is used to align the magnetic field components with a new reference frame centered on the local mean magnetic field direction. This simplifies the analysis of magnetic fluctuations by separating the components parallel and perpendicular to the mean field. By transforming to this reference frame, we can isolate the transverse components (B_T and B_N), which are crucial for studying magnetic helicity. This alignment is supposed to ensure that the calculations of reduced magnetic helicity are more precise in the plane, which is something we will verify. The rotation matrix analytical derivation is given in Appendix D.

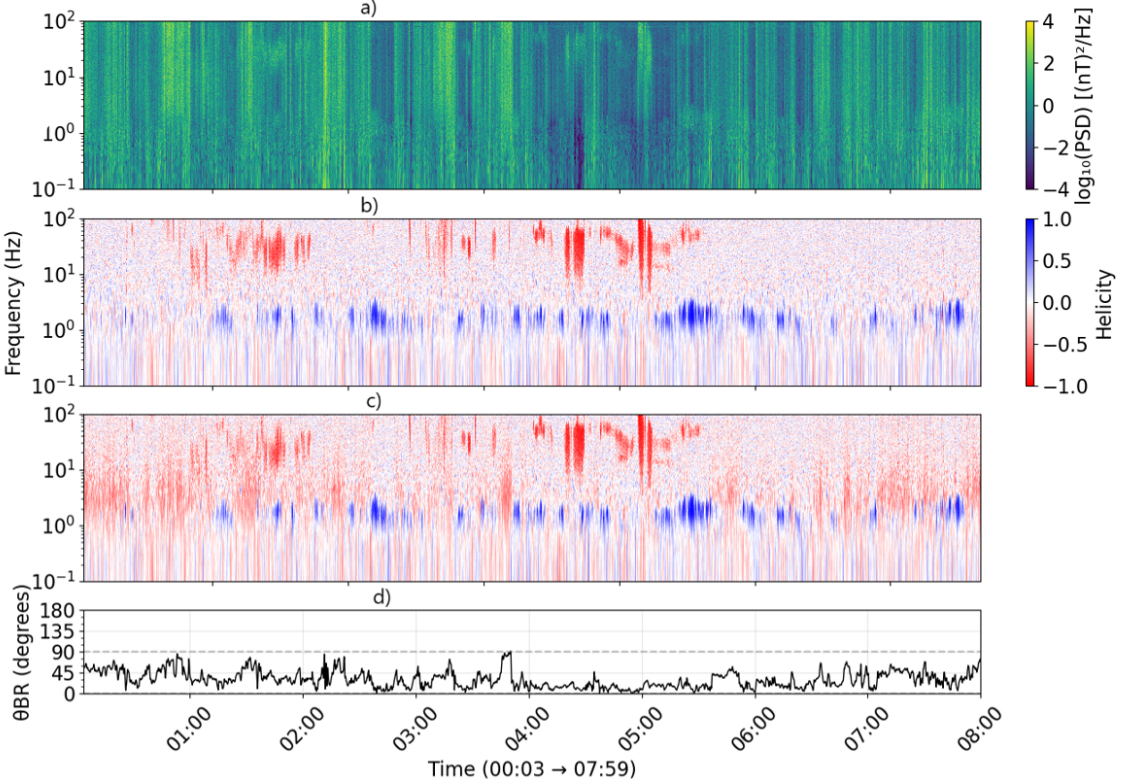


Figure 5: Segment size : 8192 points ; Overlap : 6553.6 points Data from 4 April 2024 : **a)** Power Spectral Density Spectrogram ; **b)** Magnetic Helicity Spectrogram with rotation ; **c)** Magnetic Helicity Spectrogram without rotation ; **d)** Magnetic Field - Radial Direction Angle

Rotation Matrix Analysis

To ensure the relevance of the rotation, we plot in Figure 5d) the angle between the background magnetic field and the radial direction, along with the spectrogram of helicity with and without rotation in panels b) and c). Without rotation, we observe regions where negatively polarized waves (red) appear precisely when the

angle approaches 90 degrees. These waves vanish after rotation, indicating that the transformation helps reduce contributions from undesirable directions. This behavior is consistently observed on other days, as shown in Appendix E.

This observation highlights the anisotropic nature of turbulent fluctuations: when the magnetic field is not aligned with the radial direction, fluctuations with a strong perpendicular component (relative to the field) appear more prominently in the helicity spectrogram, leading to the observed red regions. By aligning the field, the rotation filters out these contributions, allowing a clearer analysis of the energy cascade and dissipation processes.

3 Results

3.1 Cascade Interruption

To ensure that cyclotron waves are indeed involved in interrupting the cascade and dissipating energy, the PSD spectra related to these waves are extracted. Using the Mean Helicity over Time (Figure 12a) for April 4, 2024, in Appendix F, a threshold ($\sigma_m > 0.2$) is selected where all waves around $f_c = 0.6\text{Hz}$ are considered. The average helicity is plotted for these thresholds (Figure 6). For cyclotron waves ($\sigma_m > 0.2$), the observed peak clearly indicates left-polarized waves (See other days Appendix G).

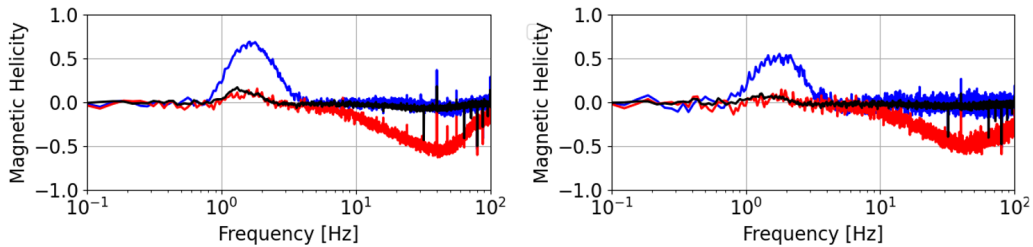


Figure 6: Segment size : 8192 points ; Overlap : 6553.6 points Data from 4 April 2024 / **Left** : PSD with all segments (4462 segments), blue segments (cyclotron) = 578, red segments (whistler) = 417, remaining segments = 3467 ; **Right** : PSD above noise (3467 segments), blue segments (cyclotron) = 157, red segments (whistler) = 220, remaining segments = 2293

With this identification of waves, we can now plot the average PSD during times when ion cyclotron waves are present and compare it to times when there are no cyclotron waves (Figure 7). For periods with cyclotron waves (blue), an energetic bump precedes a sharp energy drop. Furthermore, for the rest of the cascade in the kinetic domain, the level of fluctuations is significantly lower than the one when no waves are present, thus indicating that energy has indeed dissipated.

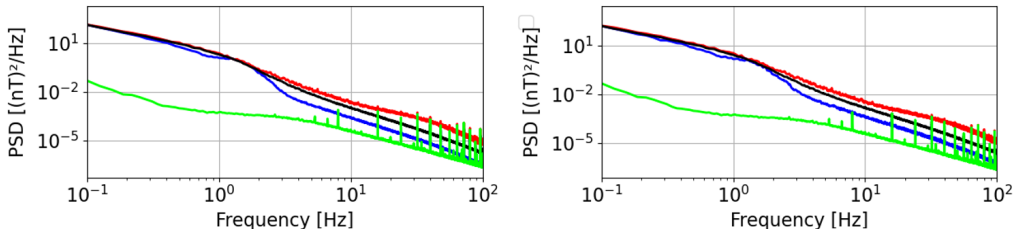


Figure 7: Segment size: 8192 points; Overlap: 6553.6 points. Data from 4 April 2024. **Left:** Reduced magnetic helicity with all segments (4462 segments) ; **Right:** Reduced magnetic helicity above noise (3467 segments). The PSD is shown for times when no waves are present (black), times with ion cyclotron waves (blue), and times with whistler waves (red). The noise level is indicated in green.

3.2 Whistler Waves Considerations

Another type of wave that was not initially planned to be studied is whistler waves. These waves are present in the PSD and helicity spectrograms (Figure 5) at frequencies close to $f = 20 - 30\text{ Hz}$ [14]. Using a threshold of

$\sigma_m < 0.2$, Figure 6 shows right-hand polarization (in red). The PSD spectrum (Figure 7) does not exhibit any clear signs, except for a slight "bump" around 50 Hz. Investigating higher frequencies, which was not possible here, could reveal whether the whistler waves impact the turbulence at electron scales.

In contrast, Figure 14, which corresponds to the data from September 6, 2022, reveals a more extended bump. This is due to a stronger intensity of whistler waves on that particular day.

For this type of wave, it is expected to observe a drop following a bump [13] and then a clear halt in the cascade, which is not seen here. To further investigate, it might be interesting to try using data with a higher sampling frequency.

4 Conclusion & Perspectives

This study successfully confirmed the role of ion cyclotron waves in interrupting the turbulent energy cascade in the solar wind, using the merged dataset from Solar Orbiter's MAG and SCM instruments. By analyzing the reduced magnetic helicity and power spectral density, we identified left-handed circularly polarized waves near the ion cyclotron frequency (≈ 0.6 Hz), which correlate with a sharp energy drop in the kinetic regime. This observation aligns with Bowen's findings, validating the universality of cyclotron-mediated dissipation in both near-Sun and inner heliospheric environments.

The implementation of a rotation matrix to align fluctuations with the local magnetic field significantly improved helicity analysis by filtering anisotropic contributions, particularly during intervals of high field-radial misalignment. Additionally, the selection of only spectra above the noise threshold improved result reliability, though further refinement (e.g., adaptive thresholding) could enhance this process.

While cyclotron waves exhibited a clear association with energy dissipation, whistler waves showed ambiguous spectral signatures, suggesting their role in turbulence dynamics requires further investigation with higher-resolution data capable of probing smaller electron-scale structures.

Several questions remain unanswered, and some avenues would have deserved further exploration. Indeed, it would have been interesting to apply these tools to a broader set of Solar Orbiter data to compare different plasma environments. Additionally, taking into account solar wind velocity measurements to correct for Doppler shifts would have refined ion cyclotron frequency determination. It would also have been valuable to combine magnetic field analysis with ion and electron measurements, such as density and temperature, to quantify heating rates associated with wave dissipation.

This work lays the foundation for developing a user-friendly interface to analyze magnetic turbulence in the solar wind, designed for researchers in heliophysics. It highlights the importance of multi-instrument datasets for studying kinetic-scale phenomena and establishes a framework for future turbulence research. This work will be further developed through an M1 internship.

5 Appendices

5.1 Appendix A: Magnetic Field Evolution of Others Days

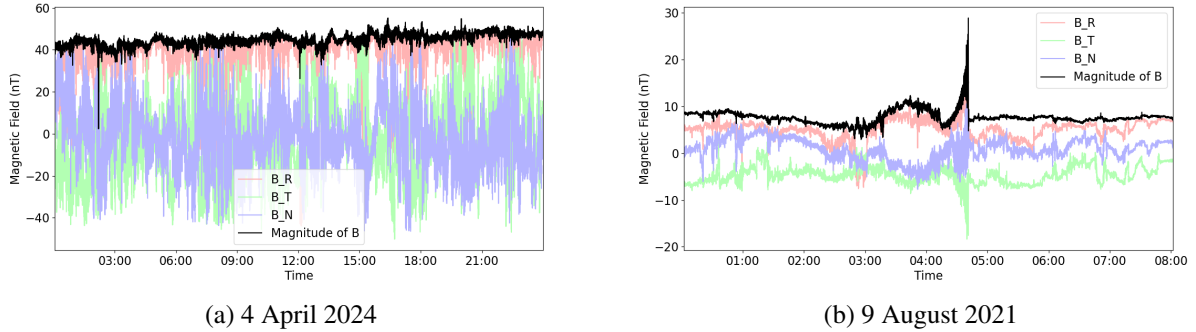


Figure 8: Data of Magnetic Field Evolution in RTN coordinates.

5.2 Appendix B: Reduced Magnetic Helicity Demonstration

The vector potential for a fluctuating magnetic field can be obtained by uncurling the definition of the vector potential [15].

$$\mathbf{B} = \nabla \times \mathbf{A} \quad (5)$$

We multiply Eq. (5) by the curl operator,

$$\nabla \times (\nabla \times \mathbf{A}) = \nabla(\nabla \cdot \mathbf{A}) - \nabla^2 \mathbf{A}$$

Here the first term on the right hand side vanishes under the Coulomb gauge

$$\nabla \cdot \mathbf{A} = 0$$

in which case we obtain

$$\nabla \times \mathbf{B} = -\nabla^2 \mathbf{A} \quad (6)$$

For a plane wave geometry $\mathbf{B} = \mathbf{b} \exp[i\mathbf{k} \cdot \mathbf{r}]$ and $\mathbf{A} = \mathbf{a} \exp[i\mathbf{k} \cdot \mathbf{r}]$ Eq. (6) becomes

$$i\mathbf{k} \times \mathbf{b} = -k^2 \mathbf{a}$$

where $k = |\mathbf{k}|$. The vector potential amplitude \mathbf{a} is therefore given as

$$\mathbf{a} = -\frac{i}{k^2} \mathbf{k} \times \mathbf{b} \quad (7)$$

The magnetic helicity density can be determined by building a product between \mathbf{a} and \mathbf{b} ,

$$h = \langle \mathbf{a}^\dagger \cdot \mathbf{b} \rangle$$

where the angular bracket denotes the operation of averaging either in the time domain or in the frequency domain. Using the expression of the vector potential \mathbf{a} (7), the estimator for the helicity density is given as a combination of cross correlation of magnetic field fluctuations between different components:

$$\langle \mathbf{a}^\dagger \cdot \mathbf{b} \rangle = -\frac{i}{k^2} \left[k_x \left(\langle b_y^* b_z \rangle - \langle b_z^* b_y \rangle \right) + k_y \left(\langle b_z^* b_x \rangle - \langle b_x^* b_z \rangle \right) + k_z \left(\langle b_x^* b_y \rangle - \langle b_y^* b_x \rangle \right) \right] \quad (8)$$

Now, we consider \mathbf{k} in the direction of \mathbf{R} and replace x, y, z with R, T, N . By simplifying and removing the last two terms, we get:

$$\langle \mathbf{a}^\dagger \cdot \mathbf{b} \rangle = -\frac{i}{k_R} \left(\langle b_T^* b_N \rangle - \langle b_N^* b_T \rangle \right)$$

The term $\langle b_T^* b_N \rangle - \langle b_N^* b_T \rangle$ can be rewritten explicitly in terms of its imaginary part as:

$$\langle b_T^* b_N \rangle - \langle b_N^* b_T \rangle = 2i \operatorname{Im}[\langle b_T^* b_N \rangle]$$

This highlights the connection between the antisymmetric cross-correlation and the helicity's imaginary component.

To obtain a dimensionless measure of the reduced magnetic helicity, we normalize by the trace of the spectral matrix, $Em = \langle b_T^2 + b_N^2 \rangle$, which represents the total energy in the transverse magnetic field components. The dimensionless reduced magnetic helicity is given by [10]:

$$\langle \sigma_m \rangle = \frac{k_R \langle \mathbf{a}^\dagger \cdot \mathbf{b} \rangle}{Em} = \frac{2\operatorname{Im}\langle b_T^* b_N \rangle}{\langle b_T^2 + b_N^2 \rangle} \quad (9)$$

This normalization ensures that $\langle \sigma_m \rangle$ is bounded between -1 and 1, to observe the polarization of the magnetic fluctuations.

5.3 Appendix C: Polarization Consideration

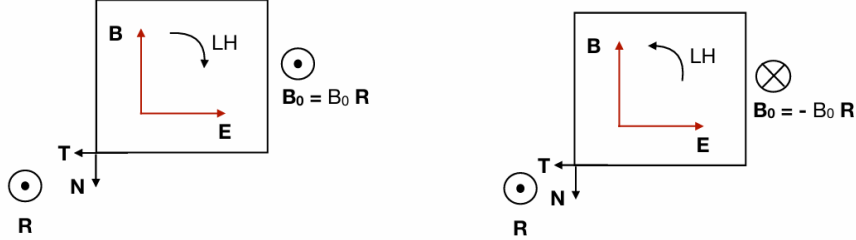


Figure 9: Reference frame to establish the wave polarization

5.4 Appendix D : Analytical Derivation of the Rotation Matrix

The rotation matrix \mathbf{R} aligns magnetic field components with a coordinate system centered on the local mean magnetic field direction \mathbf{B}_0 . This matrix is constructed from three orthonormal unit vectors that form the new coordinate system basis.

First, we calculate the mean magnetic field \mathbf{B}_0 over an interval:

$$\mathbf{B}_0 = \frac{1}{N} \sum_{i=1}^N \mathbf{B}_i \quad (10)$$

where $\mathbf{B}_i = [B_{x,i}, B_{y,i}, B_{z,i}]^T$ is the magnetic field vector at time step i .

The first unit vector \mathbf{e}_1 aligns with \mathbf{B}_0 :

$$\mathbf{e}_1 = \frac{\mathbf{B}_0}{\|\mathbf{B}_0\|}$$

where $\|\mathbf{B}_0\| = \sqrt{B_{x0}^2 + B_{y0}^2 + B_{z0}^2}$. The second unit vector \mathbf{e}_2 is obtained by normalizing the cross product of an arbitrary vector \mathbf{u} (typically $[0, 1, 0]^T$) with \mathbf{e}_1 :

$$\mathbf{e}_2 = \frac{\mathbf{u} \times \mathbf{e}_1}{\|\mathbf{u} \times \mathbf{e}_1\|}$$

The third unit vector \mathbf{e}_3 completes the orthonormal basis:

$$\mathbf{e}_3 = \mathbf{e}_1 \times \mathbf{e}_2$$

The rotation matrix \mathbf{R} is then constructed as:

$$\mathbf{R} = \begin{bmatrix} \mathbf{e}_1^T \\ \mathbf{e}_2^T \\ \mathbf{e}_3^T \end{bmatrix} \quad (11)$$

and the rotated magnetic field vectors are obtained by:

$$\mathbf{B}_{\text{rot}} = \mathbf{B}_{\text{data}} \cdot \mathbf{R} \quad (12)$$

5.5 Appendix E : Spectrograms of others days

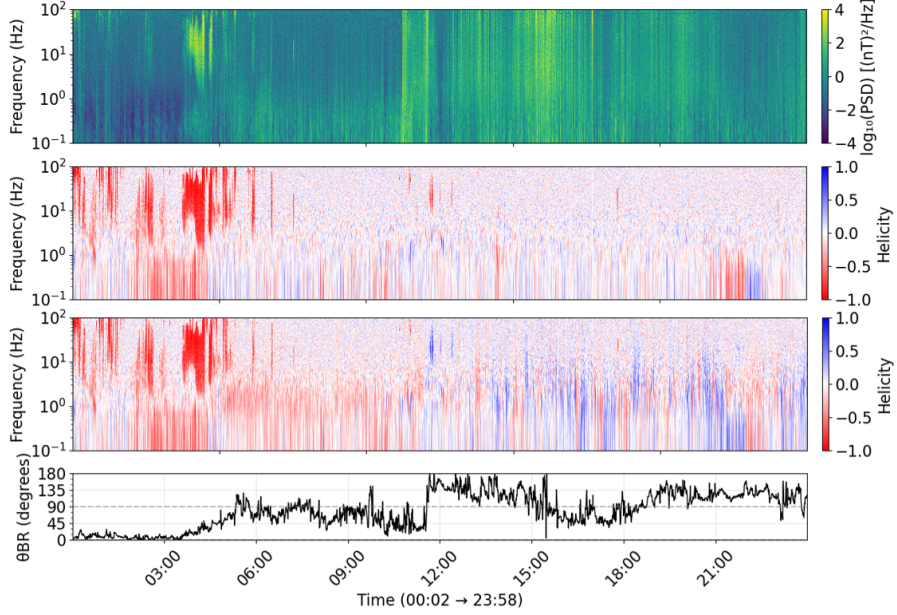


Figure 10: Data from 6 September 2022, Top to Bottom : a) Power Spectral Density Spectrogram ; b) Magnetic Helicity Spectrogram with rotation ; c) Magnetic Helicity Spectrogram without rotation ; d) Magnetic Field - Radial Direction Angle

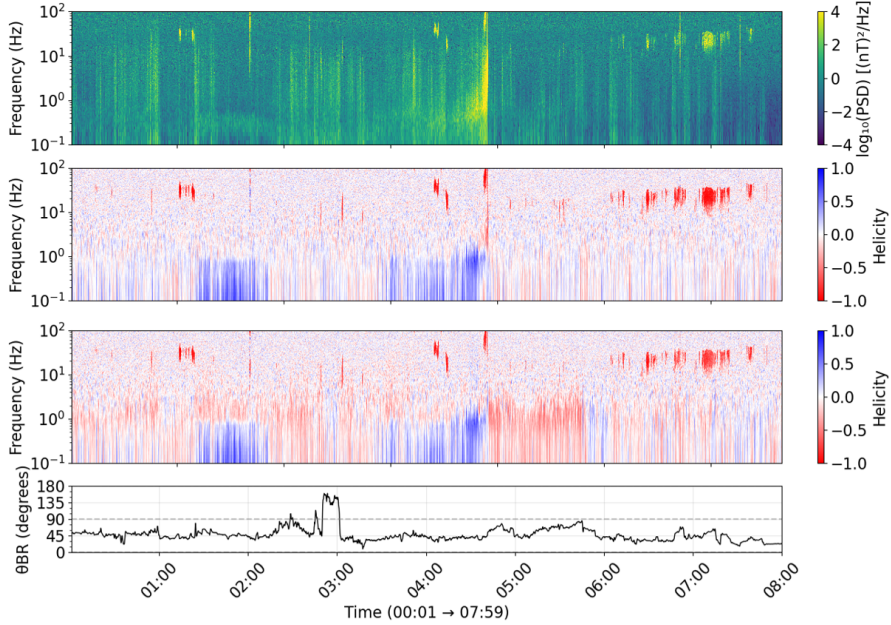


Figure 11: Data from 9 August 2021, Top to Bottom : a) Power Spectral Density Spectrogram ; b) Magnetic Helicity Spectrogram with rotation ; c) Magnetic Helicity Spectrogram without rotation ; d) Magnetic Field - Radial Direction Angle

For the first 6 September 2022, we observe very few left-polarized cyclotron waves. However, Whistler waves are present with a strong energetic signature. As for August 9, 2021, a bit of both can be observed, but too little to be significant in the following analysis.

5.6 Appendix F : Mean helicity and mean PSD over time for all days

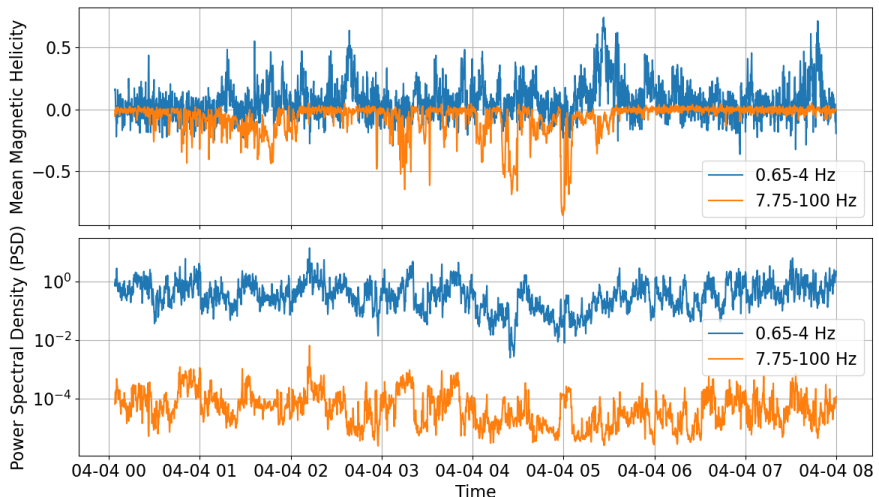


Figure 12: Magnetic Helicity and PSD in Frequency Bands vs Time from 4 April 2024

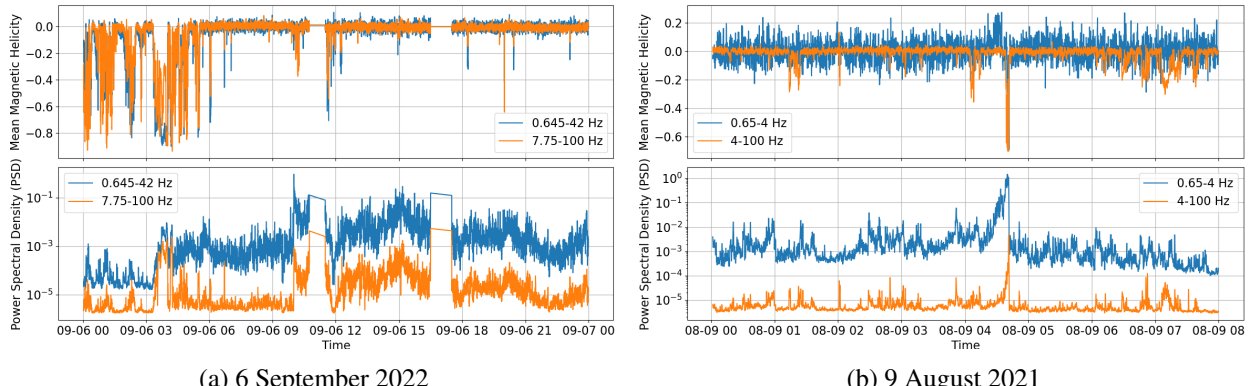


Figure 13: Data of Magnetic Field Evolution in RTN coordinates.

For each days, it's noted that certain structures clearly visible in the helicity signal (upper panel) are not detectable in the PSD (lower panel). This phenomenon is particularly interesting as it suggests that some waves, although possessing a significant magnetic helicity signature, have a relatively low energy amplitude that becomes "buried" in the overall turbulent spectrum.

In other words, the polarization signal (helicity) allows us to highlight certain coherent waves that would otherwise be undetectable in a simple energy analysis, as they are masked by the ambient turbulence. This demonstrates the importance of analyzing both helicity and spectral density to fully identify the different types of waves present in the medium.

5.7 Appendix G: PSD & Reduced Magnetic Helicity for Cyclotron and Whistler Wave Observations

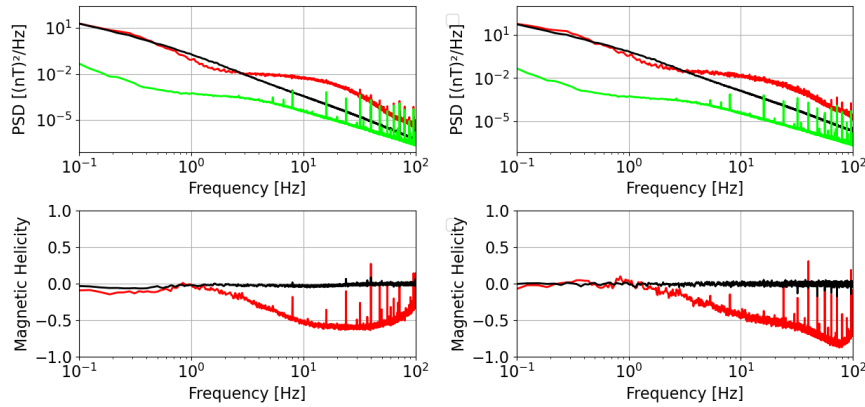


Figure 14: Segment size : 8192 points ; Overlap : 6553.6 points Data from 6 September 2022 / Left : PSD with all segments (12484 segments), blue segments (cyclotron) = 0, red segments (whistler) = 1324, remaining segments = 11160 Right : PSD above noise (2945 segments), blue segments (cyclotron) = 0, red segments (whistler) = 492, remaining segments = 2453

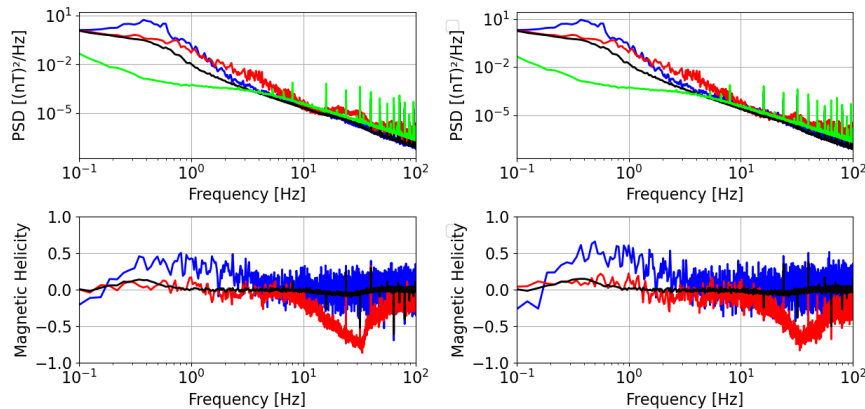


Figure 15: Segment size : 8192 points ; Overlap : 6553.6 points Data from 9 August 2021 / Left : PSD with all segments (4485 segments), blue segments (cyclotron) = 26, red segments (whistler) = 136, remaining segments = 4323 Right : PSD above noise (2688 segments), blue segments (cyclotron) = 20, red segments (whistler) = 77, remaining segments = 2591

References

- [1] Uriel Frisch. *Turbulence: The Legacy of A. N. Kolmogorov*. Cambridge University Press, Cambridge, UK, 1995. Reprinted 1996.
- [2] A. N. Kolmogorov. The local structure of turbulence in incompressible viscous fluid for very large reynolds numbers. *Proceedings: Mathematical and Physical Sciences*, 434(1890):9–13, July 1991.
- [3] Roberto Bruno and Vincenzo Carbone. The solar wind as a turbulence laboratory. *Living Reviews in Solar Physics*, 10:2, 2013. Accepted: 22 March 2013, Published: 29 May 2013, Update of lrsp-2005-4.
- [4] C. H. K. Chen, S. D. Bale, J. W. Bonnell, D. Borovikov, T. A. Bowen, D. Burgess, A. W. Case, B. D. G. Chandran, and T. Dudok de Wit. The evolution and role of solar wind turbulence in the inner heliosphere. *The Astrophysical Journal Supplement Series*, 246(2):53, 2020.

- [5] J. Zhang, S. Y. Huang, J. S. He, T. Y. Wang, Z. G. Yuan, X. H. Deng, K. Jiang, Y. Y. Wei, S. B. Xu, Q. Y. Xiong, R. T. Lin, and L. Yu. Three-dimensional anisotropy and scaling properties of solar wind turbulence at kinetic scales in the inner heliosphere: Parker solar probe observations. *The Astrophysical Journal Letters*, 924(L21):8, January 2022.
- [6] Trevor A. Bowen, Stuart D. Bale, Benjamin D. G. Chandran, Alexandros Chasapis, Christopher H. K. Chen, Thierry Dudok de Wit, Alfred Mallet, Romain Meyrand, and Jonathan Squire. Mediation of collisionless turbulent dissipation through cyclotron resonance. *Nature Astronomy*, 8:482–490, April 2024.
- [7] S. D. Bale, S. T. Badman, J. W. Bonnell, T. A. Bowen, D. Burgess, and Case et al. Highly structured slow solar wind emerging from an equatorial coronal hole. *Nature*, 576:228–231, 2019.
- [8] M. Maksimovic, S. D. Bale, T. Chust, Y. Khotyaintsev, V. Krasnoselskikh, M. Kretzschmar, D. Plette-meier, H. O. Rucker, J. Soucek, M. Steller, Š. Štverák, P. Trávníček, A. Vaivads, et al. The solar orbiter radio and plasma waves (rpw) instrument. *Astronomy & Astrophysics*, 642:A12, 2020.
- [9] Peter D. Welch. The use of fast fourier transform for the estimation of power spectra: A method based on time averaging over short, modified periodograms. *IEEE Transactions on Audio and Electroacoustics*, AU-15(2):70–73, June 1967.
- [10] T. Alberti, Y. Narita, L. Z. Hadid, D. Heyner, A. Milillo, C. Plainaki, H.-U. Auster, and I. Richter. Tracking of magnetic helicity evolution in the inner heliosphere: A radial alignment study. *Astronomy & Astrophysics*, 664:L8, 2022.
- [11] Daniele Telloni, Francesco Carbone, Roberto Bruno, Gary P. Zank, Salvatore Mancuso, and Luca Sorriso-Valvo. Ion cyclotron waves in field-aligned solar wind turbulence. *The Astrophysical Journal Letters*, 885:L5, November 2019.
- [12] Trevor A. Bowen, Alfred Mallet, Jia Huang, Kristopher G. Klein, David M. Malaspina, Michael Stevens, Stuart D. Bale, J. W. Bonnell, Christopher H. K. Chen, Anthony W. Case, and Dudok de Wit et al. Ion-scale electromagnetic waves in the inner heliosphere. *The Astrophysical Journal Supplement Series*, 246(18):66, 2020.
- [13] M. Kretzschmar, T. Chust, V. Krasnoselskikh, D. Graham, and Colombar et al. Whistler waves observed by solar orbiter/rpw between 0.5 au and 1 au. , 656:A24, 2021.
- [14] Yuguang Tong, Ivan Y. Vasko, Anton V. Artemyev, Stuart D. Bale, and Forrest S. Mozer. Statistical study of whistler waves in the solar wind at 1 au. *The Astrophysical Journal*, 878:41, 2019.
- [15] Y. Narita, G. Kleindienst, and K.-H. Glassmeier. Evaluation of magnetic helicity density in the wave number domain using multi-point measurements in space. *Annales Geophysicae*, 27:3967–3976, 2009. This work is distributed under the Creative Commons Attribution 3.0 License.